Chinese Chemical Letters 36 (2025) 110097

Contents lists available at ScienceDirect

Chinese Chemical Letters

journal homepage: www.elsevier.com/locate/cclet

Enhanced ferroptosis by a nanoparticle mimicking hemoglobin coordinate pattern with self-supplying hydrogen peroxide

Yan Gao, Zi-Lin Song, Shuang Yu, Xiu-Li Zhao, Da-Wei Chen, Ming-Xi Qiao*

School of Pharmacy, Shenyang Pharmaceutical University, Shenyang 110016, China

ARTICLE INFO

Article history:
Received 10 April 2024
Revised 3 June 2024
Accepted 5 June 2024
Available online 6 June 2024

Keywords:
Hemoglobin-mimicking
Coordination-assembly
Ferroptosis
H_2O_2 self-supply
Functionalized lipopeptide

ABSTRACT

Insufficient endogenous H_2O_2 for generation of hydroxyl radicals (•OH) has strikingly compromised anti-tumor benefits of ferroptosis. Herein, we develop a H_2O_2 self-supplying nanoparticle based on a pH-responsive lipopeptide C_{18}-pHis$_{10}$. Inspired by the coordinate pattern of hemoglobin binding heme, Fe^{2+} and tetrakis(4-carboxyphenyl)porphyrin (TCPP) were delicately encapsulated by formation of coordination compounds with His. Ascorbgyl palmitate (AscP) was also incorporated into the nanoparticles for generation of H_2O_2 by reduction $^1O_2$ produced from TCPP, meanwhile prevented Fe^{2+} from being oxidized. The protonation of pHis in acidic endo-lysosome induced the breakage of Fe^{2+}/His/TCPP coordinate interactions, leading to accelerated release of payloads and the following escape to cytoplasm. Upon laser irradiation, TCPP produces excessive $^1O_2$ followed by conversion to H_2O_2 in the presence of AscP, which is further catalyzed to lethal •OH by Fe^{2+} *via* Fenton reaction. The self-supplying H_2O_2 was found to result significantly higher accumulation of lipid peroxides and more effective tumor inhibition. Overall, this work sheds new a light on H_2O_2 self-supplying strategy to enhance ferroptosis by taking advantage of $^1O_2$ generated by photodynamic therapy (PDT).

Ferroptosis is a newly-defined non-apoptotic regulated cell death, offering a promising therapeutic alternative to the existing cancer therapies due to the circumvention of chemotherapy resistance and activation of anti-tumor immune response [1-8]. Ferroptosis is primarily induced by the hydroxyl radical (•OH) that generated from Fenton reaction ($Fe^{2+} + H_2O_2 \rightarrow Fe^{3+} + (OH)^- + {}^\bullet OH$) [9-12]. As one of the most potent reactive oxygen species (ROS), •OH directly oxidize polyunsaturated fatty acids (PUFAs)-rich phospholipids and produce highly lethal lipid peroxides (LPOs) [13-16], inducing the disruption of cell membrane and the subsequent ferroptosis [2,17-18]. Although ferroptosis has been extensively explored, it is still facing the challenge of low efficiency of •OH generation *via* Fenton reaction in cancer tissues.

The efficiency of Fenton reaction has been restricted by several factors such as H_2O_2 concentration [19-21], metal catalyst [22,23], pH and external energy field [24,25]. Among these, low H_2O_2 level within tumor microenvironment is one of the key limiting factors that needs to be properly addressed [26,27]. One approach has been reported to augment H_2O_2 level was delivery exogenous H_2O_2 generators, such as H_2O_2 prototype drug [28], glucose oxidase (GOx) [29-31], and inorganic peroxides (calcium peroxide, copper peroxide nanodots, *etc.*) [32], but low stability of these reagents in aqueous solution restricts their efficiency. The other approach is to *in situ* amplify endogenous H_2O_2 generation pathway, such as nicotinamide adenine dinucleotide phosphate (NADPH)/superoxide dismutase (SOD) [33-35], peroxidase [36,37], glutathione peroxidases (GPx) [38], and catalase [39,40]. However, due to the complex and rigorous of intracellular regulatory mechanisms, the efficacy of this approach remained to be improved.

Beside the above-mentioned approaches, a more reliable way to generate H_2O_2 is from singlet oxygen ($^1O_2$), which is usually produced by photodynamic therapy (PDT) arising from energy transfer from the excited photosensitizer to oxygen molecule upon laser irradiation [33,41-45]. Because of the empty Π_{2p}^* orbital, $^1O_2$ possesses strongly electrophilic ability that could readily react with the electron-rich compounds through electrophilic addition or electron transfer [46]. But due to the high energy barrier, a catalyst or activator is required to facilitate the above reaction processes. For example, the thiazole-based conjugated polymers were utilized to photo-catalyze H_2O_2 production from $^1O_2$ *via* a [4 + 2] cycloaddition mechanism [47]. Moreover, two electron transfer reaction in the presence of reducing agents was found to convert $^1O_2$ to H_2O_2 [46,48]. Therefore, the conversion of H_2O_2 from $^1O_2$ is assumed to be a more reliable strategy to enhance ferroptosis by PDT. Despite the intensive researches about using PDT for boosting

* Corresponding author.
E-mail address: qiaomingxi@163.com (M.-X. Qiao).

https://doi.org/10.1016/j.cclet.2024.110097
1001-8417/

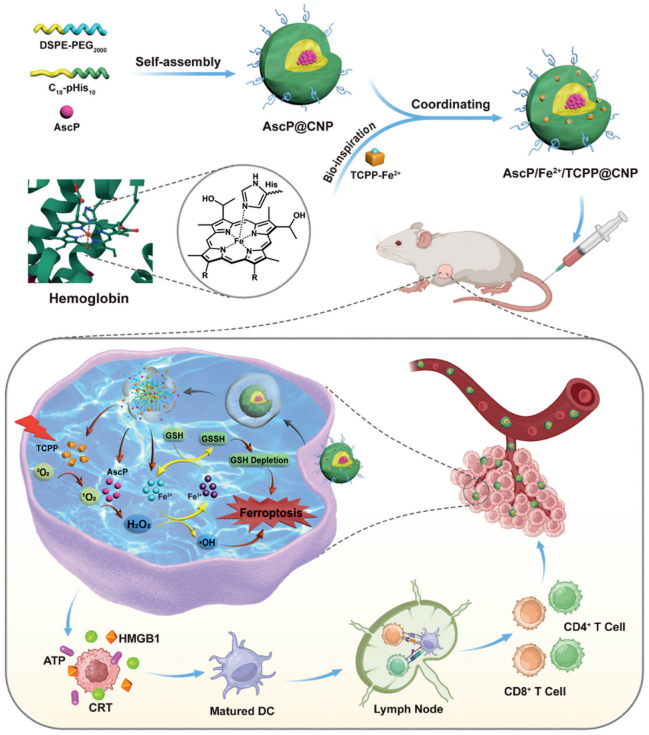

Scheme 1. Schematic illustration of AscP/Fe^{2+}/TCPP@CNP nanoparticle to boost the ferroptosis *via* H_2O_2 self-supplying. Top panel: Self-assembly mode of AscP/Fe^{2+}/TCPP@CNP by mimicking hemoglobin coordinate pattern. Bottom panel: The *in vivo* anti-tumor mechanism of AscP/Fe^{2+}/TCPP@CNP. After accumulated in tumor tissue *via* enhanced permeability and retention effect and subsequent internalized by tumor cells, TCPP produced excessive $^1O_2$ upon laser irradiation followed by conversion to H_2O_2 in the presence of AscP, and was further catalyzed to lethal $^{\bullet}OH$ by Fe^{2+} *via* Fenton reaction. The produced Fe^{3+} also contributed to ferroptosis by consuming GSH and regenerating Fe^{2+}. The ferroptotic tumor cells could activate anti-tumor immune response to further enhance the therapeutic effect.

ferroptosis, few studies have focused on the conversion of $^1O_2$ to H_2O_2 [48-50]. Therefore, the study would draw researchers' attention to a new perspective of using PDT to enhance ferroptosis.

Herein, a proof-of-concept study was conducted by developing a pH-responsive amphiphilic lipopeptide C_{18}-$pHis_{10}$ for co-delivery of ferrous ion (Fe^{2+}), photosensitizer tetrakis(4-carboxyphenyl)porphyrin (TCPP) and ascorbgyl palmitate (AscP) (Scheme 1). As TCPP possesses the basic porphyrin nucleus structure, Fe^{2+} and TCPP were encapsulated into the lipopeptide assemblies by coordination interaction with His, which mimicked the coordinate pattern of hemoglobin binding heme. AscP was further encapsulated in the hydrophobic domain of the lipopeptide assemblies. As a reducing agent, AscP played double roles in the nanoparticle. One is to prevent Fe^{2+} from being oxidized and therefore maintain the stability of the nanoparticle. The other more important one is to reduce $^1O_2$ to generate H_2O_2 for further catalyzed to lethal $^{\bullet}OH$. The functionalized lipopeptide was expected to respond to the acidic endo-lysosome environment causing the breakage of Fe^{2+}/His/TCPP coordinate interaction, thereby resulted the disruption of the nanoparticle and the fast release of payloads. Upon laser irradiation, TCPP produced the excessive $^1O_2$ followed by conversion to H_2O_2 in the presence of AscP, which was further catalyzed to lethal $^{\bullet}OH$ by Fe^{2+} *via* Fenton reaction. The byproduct of Fenton reaction of Fe^{3+} also contributed to ferroptosis by consuming intracellular glutathione (GSH) which compromised lipid peroxides scavenging system and regenerated the catalyst of Fe^{2+} for Fenton reaction.

The pH-responsive amphiphilic lipopeptide C_{18}-$pHis_{10}$ was synthesized by using stearic acid, $pHis_{10}$(Trt) as starting materials. The detailed synthesis procedure, characterization results were provided in Figs. S1 and S2 (Supporting information). The synthesized lipopeptide exhibited significantly buffering capacity in pH range from 7.4 to 5.5 (Fig. S3 in Supporting information), and increased critical micelle concentration value as pH decrease (Fig. S4 in Supporting information) due to the protonation of imidazole groups of $pHis_{10}$ in acidic environment. This indicated superior ability of lipopeptide in effectively triggered release and endo-lysosome escape of the payloads [51,52].

Inspired by the coordinate pattern of hemoglobin, the functionalized lipopeptide was developed to incorporate Fe^{2+} and photosensitizer TCPP with porphyrin structure to construct the coordination-assembled nanoparticle (Fe^{2+}/TCPP@CNP). The H_2O_2 converser of AscP was further co-encapsulated in the hydrophobic domain of the nanoparticle (AscP/Fe^{2+}/TCPP@CNP). The AscP/Fe^{2+}/TCPP@CNP showed as a reddish-brown colloidal solution, while exhibited distinct red-fluorescence under laser irradiation (Fig. S5 in Supporting information). Transmission electron microscopy (TEM) images indicated the formation of spherical nanoparticle with the size around 120 nm (Fig. 1a). Dynamic light scattering (DLS) analysis (Fig. 1a) revealed an average particle size of 118.35 ± 3.57 nm and a narrow polydispersity index (PDI) of 0.163 ± 0.08. The zeta-potential of AscP@CNP was -2.58 ± 0.36 mV, and that for AscP/Fe^{2+}/TCPP@CNP was decreased to -19.28 ± 0.96 mV due to the incorporation of negatively charged TCPP.

Iron is known to coordinate both with histidine residues and with the interior pyrrole nitrogen of porphyrin to form iron porphyrins, which are common existent in natural biomolecules and play indispensable roles in sustaining physiological function [53]. The change of zeta-potential from -2.58 ± 0.36 mV to -19.28 ± 0.96 mV indicated the coordinative encapsulation of TCPP indirectly. To in-depth study the coordinative interactions between TCPP/Fe^{2+}/His, the coordination structure was first simulated by density functional theory (DFT, M06–2X) calculations. The results showed that all the bond lengths were around 2.1 Å (Fig. 1b), indicating the potential of Fe^{2+} in coordination with the imidazole groups from $pHis_{10}$ peptide and the center porphyrin ring from TCPP. The coordination between Fe^{2+} and His was investigated by Fourier transform infrared (FT-IR), where the characteristic bands of -NH and ring from imidazole group in Fe^{2+}-lipopeptide complexes were all significantly shifted from 3165.1 and 1534.8 cm^{-1} to 3155.5 and 1523.7 cm^{-1}, respectively, compared to free lipopeptide (Fig. 1c, Table S1 in Supporting information), suggesting that the Fe^{2+} coordinated to the imidazole groups from $pHis_{10}$. The coordinative interactions within TCPP/Fe^{2+}/His was *in situ* verified by both ultraviolet–visible (UV–vis) absorption spectra and fluorescence spectra. UV–vis absorption spectra of free TCPP showed one intense Soret band (414 nm) and four Q-bands (500–700 nm). In contrast, the Soret band redshifted to 415 nm and Q band number was reduced from four to two in AscP/Fe^{2+}/TCPP@CNP (Fig. 1d). Additionally, the maximum emission wavelength of AscP/Fe^{2+}/TCPP@CNP redshifted by 4 nm compared to free TCPP (Fig. 1e). Taken together, these findings confirmed the multi-component coordinative interactions of TCPP and His in concert with Fe^{2+} within the nanoparticle.

The encapsulation efficiency (EE) of the three payloads in lipopeptide nanoparticle were all higher than 93%, demonstrated the superior performance of the lipopeptide in co-encapsulation of multiple components with diverse physio-chemical properties (Table S2 in Supporting information). *In vitro* release profile was investigated in phosphate buffer saline (PBS) solutions (0.01 mol/L) at different pH values (Fig. 1f). The nanoparticle exhibited negligible leakage (<15%) after 24 h incubation at pH 7.4 but an accelerated release profiles at acidic condition. Specifically, the cumulative release amount of AscP, Fe^{2+} and TCPP increased

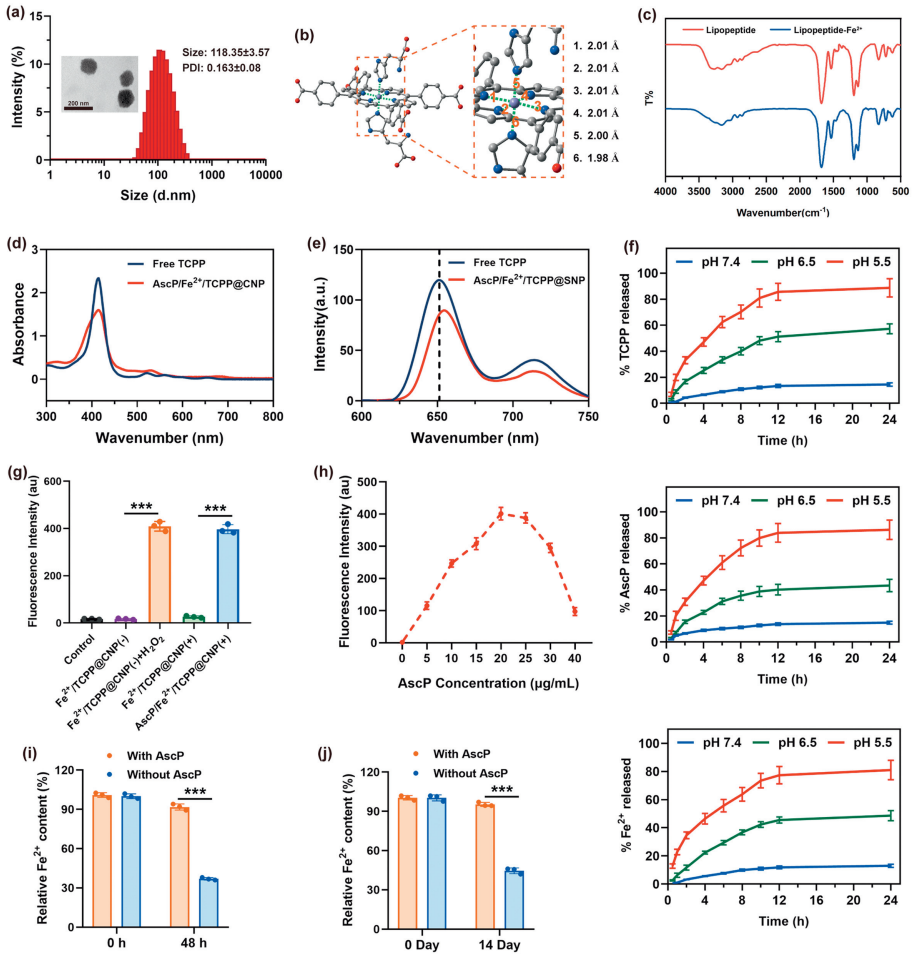

Fig. 1. Characterizations for AscP/Fe^{2+}/TCPP@CNP. (a) TEM image and particle size analyzed by DLS of AscP/Fe^{2+}/TCPP@CNP (scale bar: 200 nm). (b) Coordination conformations of TCPP/Fe^{2+}/His and the bonds lengths. (c) FT-IR spectra of lipopeptide and corresponding complex with Fe^{2+}. UV–vis absorption spectra (d) and fluorescence spectra (e) of free TCPP and AscP/Fe^{2+}/TCPP@CNP, respectively. (f) *In vitro* release profiles of AscP, Fe^{2+} and TCPP from nanoparticle at different pH values (7.4, 6.5 and 5.5), respectively ($n = 3$). (g) The $^{\bullet}OH$ generation ability of different nanoparticles ($n = 3$). (h) The influence of AscP concentration on the production of $^{\bullet}OH$ from the AscP/Fe^{2+}/TCPP@CNP ($n = 3$). The relative Fe^{2+} content in the platform after 10-fold dilution by PBS (pH 7.4, 0.01 mol/L) containing 10% FBS (i) and storage for 14 days at 4 °C (j). Data are presented as mean ± standard deviation (SD). $^{***}P < 0.001$.

from 14.82% ± 1.14% to 86.21% ± 3.06%, from 13.87% ± 1.15% to 85.12% ± 3.59% and from 14.42% ± 1.33% to 88.74% ± 3.35%, respectively, as pH decrease from pH 7.4 to 5.5. The efficient and synchronous release of the payloads from nanoparticle could be primarily attributed to the protonation of imidazole residues in histidine, leading to the breaking of multi-component coordinative interactions in acidic environment.

The extracellular $^{\bullet}OH$ production of the AscP/Fe^{2+}/TCPP@CNP was performed using HKOH-1 as sensor [54]. As illustrated in Fig. 1g, the fluorescence intensity induced by $^{\bullet}OH$ in Fe^{2+}/TCPP@CNP(-)+H_2O_2 remarkably higher than Fe^{2+}/TCPP@CNP(-) and control group, indicating the Fenton reaction catalysis ability of the nanoparticle. The negligible $^{\bullet}OH$ signal in Fe^{2+}/TCPP@CNP(+) group indicated that $^1O_2$ could not be spontaneously converted to H_2O_2. Moreover, fluorescence intensity from AscP/Fe^{2+}/TCPP@CNP(+) was distinctly higher than that from Fe^{2+}/TCPP@CNP(+), indicating that $^1O_2$ excited by TCPP could be converted to H_2O_2 in the presence of AscP for $^{\bullet}OH$ generation. The influence of AscP content on the $^{\bullet}OH$ generation was further investigated. As shown in Fig. 1h, as AscP concentration increased, the production of $^{\bullet}OH$ gradually increased, with maximum fluorescence intensity appeared at the concentration of 20 μg/mL. Further increase of AscP led to a quick decrease in the production of $^{\bullet}OH$, which was probably attributed to the consumption of the generated H_2O_2 or $^{\bullet}OH$ by the excessive amount of AscP. Collectively, these results showed that the reducing agent of AscP could catalyze the conversion of H_2O_2 from $^1O_2$ excited by PDT.

AscP was also found to play a role in prevention Fe^{2+} from being oxidized to Fe^{3+}. As shown in Figs. 1i and j, the nanoparticle with AscP exhibited constant Fe^{2+} level after storage for 14 days at 4 °C or 10-fold dilution by PBS (pH 7.4, 0.01 mol/L) containing 10% fetal bovine serum (FBS) in contrast to that without AscP exhibiting a significant decrease in Fe^{2+} level ($P < 0.001$). It is well known that Fenton reaction is in fact initiated by Fe^{2+} rather than the oxidized Fe^{3+}, therefore the satisfactory stability of the nanoparticle benefit from the AscP endowed the nanoparticle with the potential to boost the Fenton reaction and subsequent ferroptosis induction.

Both confocal laser scanning microscopy (CLSM) (Fig. 2a) and flow cytometry (FCM) (Fig. 2b) results showed that the nanoparticle was efficiently internalized by 4T1 breast cancer cells within 4 h. In addition, AscP/Fe^{2+}/TCPP@CNP displayed a much broader distribution of TCPP red fluorescence and much less orange signal resulting from the overlap of TCPP and LysoTracker Green, indicating the effectively endo-lysosome escape of TCPP (Fig. 2c). The "proton sponge" effect from $pHis_{10}$ was verified with the help of bafilomycin A1 (proton pump inhibitor). As CLSM image shown (Fig. 2d), bafilomycin A1 treatment significantly decreased the

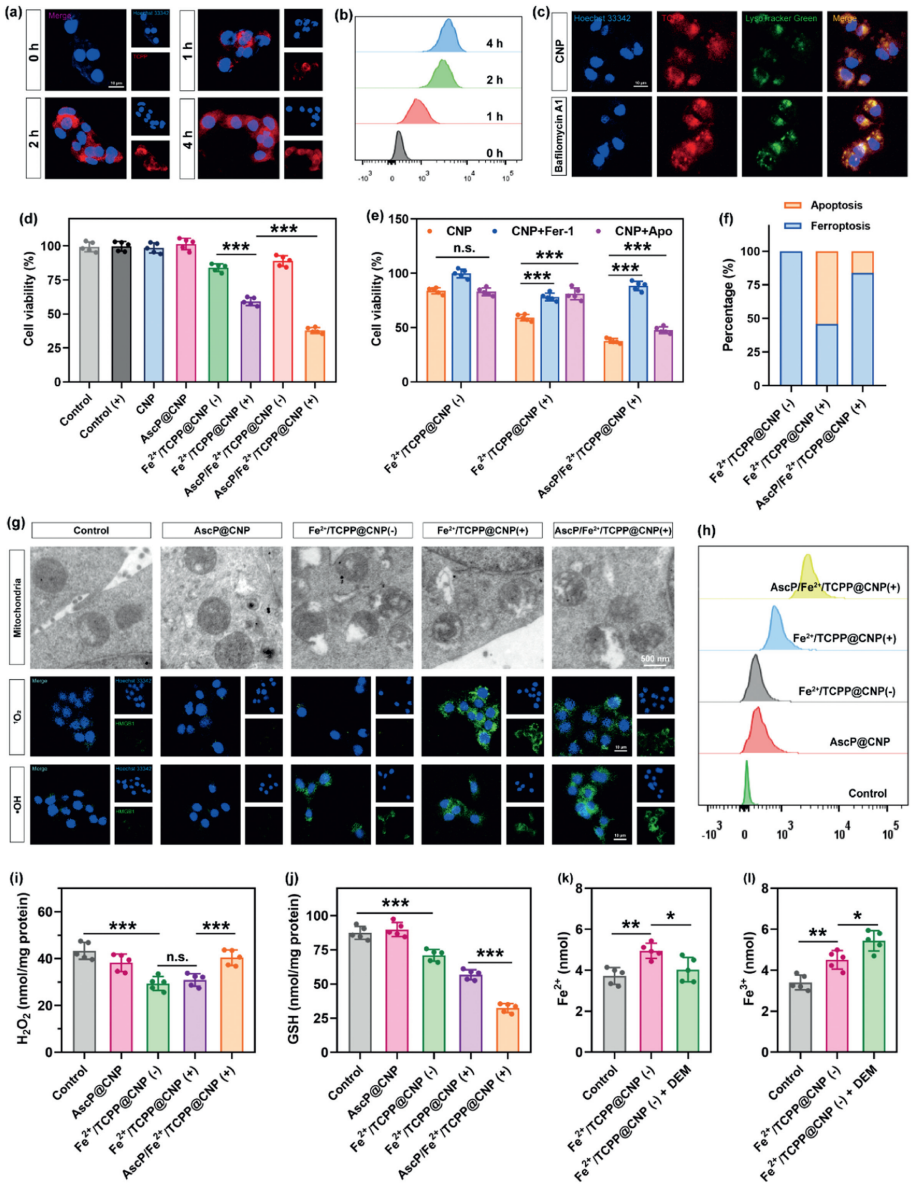

Fig. 2. Intracellular trafficking and *in vitro* efficacy of AscP/Fe^{2+}/TCPP@CNP. Internalization behavior of AscP/Fe^{2+}/TCPP@CNP against 4T1 breast cancer cells detected by CLSM (scale bar: 10 μm) (a) and FCM (b), respectively. (c) Colocalization analysis of TCPP and lysosome investigated by CLSM (scale bar: 10 μm). (d) Cell viability of 4T1 breast cancer cells after treated by different nanoparticles for 48 h ($n = 5$). (e) Cell viability of different nanoparticles in presence of ferroptosis inhibitor of Fer-1 or apoptosis inhibitor of Apo ($n = 5$). (f) The proportion of ferroptosis and apoptosis induce by different nanoparticles. (g) The mitochondria morphology (scale bar: 500 nm) captured by TEM, the $^1O_2$ and $^{\cdot}OH$ level (scale bar: 10 μm) in 4T1 breast cancer cells detected by CLSM after different nanoparticles treatment. (h) LPOs accumulation in 4T1 breast cancer cells after treated by different nanoparticles measured by FCM. Intracellular H_2O_2 (i) and GSH (j) level of 4T1 breast cancer cells after treated by different nanoparticles ($n = 5$). The Fe^{2+} (k) and Fe^{3+} (l) content in 4T1 breast cancer cells after treated by Fe^{2+}/TCPP@CNP(-) with/without GSH depleting agent DEM pretreatment ($n = 5$). Data are presented as mean ± SD. n.s., no significance. $^*P < 0.05$, $^{**}P < 0.01$, $^{***}P < 0.001$.

distribution of red signal in the cytoplasm, demonstrating that "proton sponge" effect contributed to the endo-lysosomal escape of TCPP.

The *in vitro* cytotoxicity of AscP/Fe^{2+}/TCPP@CNP against 4T1 was shown in Fig. 2d, the blank nanoparticle (CNP) and laser irradiation alone (control (+)) exhibited negligible toxicity, indicating the excellent biocompatibility of the nanoparticle. AscP@CNP treatment caused a slight but not significant increase in cell viability compared to control. AscP/Fe^{2+}/TCPP@CNP(+) treatment resulted in the strongest inhibition on the cell viability, which was significantly ($P < 0.001$) higher than Fe^{2+}/TCPP@CNP(+), indicating the positive role of AscP in boosting the anti-tumor efficacy.

The cytotoxicity mechanism of AscP/Fe^{2+}/TCPP@CNP was further studied. As the result shown (Fig. 2e), the cytotoxicity of Fe^{2+}/TCPP@CNP(-) was completely counteracted by ferroptosis inhibitor (Fer-1), but was not affected by apoptosis inhibitor (Apo). In contrast, both Fer-1 and Apo pretreatment remarkably alleviated the cytotoxicity of Fe^{2+}/TCPP@CNP(+) and AscP/Fe^{2+}/TCPP@CNP(+), respectively, indicating a hybrid cell death involving both ferroptosis and apoptosis. However, it was worth noting that AscP/Fe^{2+}/TCPP@CNP(+) induced higher proportion of ferroptosis and lower proportion of apoptosis than Fe^{2+}/TCPP@CNP(+) (Fig. 2f). Meanwhile, AscP/Fe^{2+}/TCPP@CNP(+) treatment resulted in significant mitochondria morphology changes (membrane density increase, volume decrease, crest disappearance and outer membrane rupture) (Fig. 2g) and higher accumulation of lipid peroxides (LPOs) (Fig. 3h) than that of Fe^{2+}/TCPP@CNP(+). These results confirmed that AscP enhanced

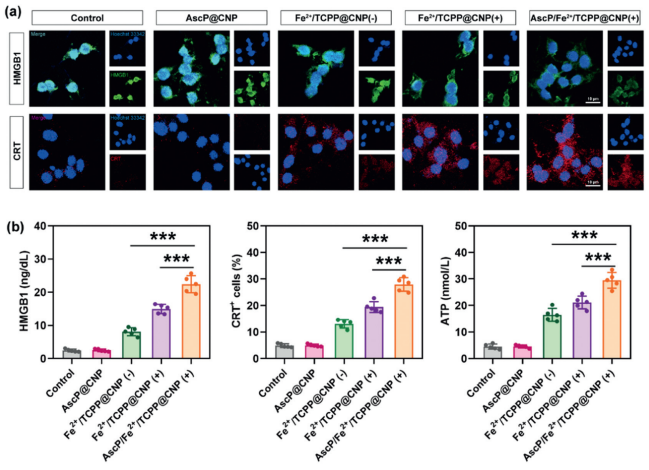

Fig. 3. The evaluation of the *in vitro* ICD effect induced by AscP/Fe^{2+}/TCPP@CNP. (a) CRT exposure and HMGB1 release after treated by different nanoparticles observed by CLSM (scale bar: 10 μm). (b) Quantitate analysis of HMGB1 release, CRT-positive cells and ATP secretion after treated by different nanoparticles ($n = 5$). Data are presented as mean ± SD. $^{***}P < 0.001$.

the anti-tumor efficacy of AscP/Fe^{2+}/TCPP@CNP(+) *via* transforming the cell death pathway induced by TCPP from apoptosis to the more lethal ferroptosis.

The intracellular $^{\bullet}OH$ levels after treated by the nanoparticles were detected with HKOH-1r as the specific probe. As shown in Fig. 2g, Fe^{2+}/TCPP@CNP(-) treatment resulted comparable increase in intracellular $^{\bullet}OH$ signal with Fe^{2+}/TCPP@CNP(+), which was caused by the Fenton reaction catalyzed by Fe^{2+}. AscP/Fe^{2+}/TCPP@CNP(+) treatment significant augmented $^{\bullet}OH$ fluorescence intensity in the cells comparing with Fe^{2+}/TCPP@CNP(+), demonstrating a prooxidant-like effect of AscP for generation of $^{\bullet}OH$ when it combined with TCPP. Fe^{2+}/TCPP@CNP(+) treated cells exhibited comparable intracellular H_2O_2 level with Fe^{2+}/TCPP@CNP(-), proving that the $^1O_2$ excited by PDT could not be spontaneously converted to H_2O_2 (Fig. 2i). AscP/Fe^{2+}/TCPP@CNP(+) treatment resulted 1.31-fold increase of intracellular H_2O_2 comparing with Fe^{2+}/TCPP@CNP(+) ($P < 0.001$) even though AscP@CNP caused a slight decrease of intracellular H_2O_2 level. Meanwhile, the $^1O_2$ fluorescence intensity in the cells treated by AscP/Fe^{2+}/TCPP@CNP(+) was significantly lower than that treated by Fe^{2+}/TCPP@CNP(+) (Fig. 2g). These results provided the evidence that AscP could convert $^1O_2$ to H_2O_2 so as to providing the substrate for Fenton reaction, thereby enhanced the production of $^{\bullet}OH$ and boosted the ferroptosis induction.

To validate the effect of AscP/Fe^{2+}/TCPP@CNP on GSH consumption, the intracellular GSH content was detected after treatment. As shown in Fig. 2j, Fe^{2+}/TCPP@CNP(-) resulted significant GSH decrease compared to the untreated cells ($P < 0.001$). The addition of GSH-depleting agent diethyl maleate (DEM) dramatically ($P < 0.05$) declined the intracellular Fe^{2+} level (Fig. 2k), meanwhile, the Fe^{3+} level in the cells was significantly ($P < 0.05$) increased (Fig. 2l). Taken together, the by-product Fe^{3+} of the Fenton reaction could destroy the antioxidant defense system in the tumor cell *via* consuming GSH and produce a Fe^{2+} regeneration cycle, contributing to the enhanced ferroptosis.

The immunological cell death (ICD) effect of the nanoparticle was further evaluated by monitoring the typical biomarkers of calreticulin (CRT), high mobility group protein B1 (HMGB1) and adenosine triphosphate (ATP). As the confocal images shown (Fig. 3a), AscP/Fe^{2+}/TCPP@CNP(+) treatment induced most distinctive CRT exposure and translocations of HMGB1, followed by Fe^{2+}/TCPP@CNP(+), Fe^{2+}/TCPP@CNP(-) and AscP@CNP. Quantitative analysis results (Fig. 3b) showed that the percentage of CRT-positive cells, the extracellular release of HMGB1 and the ATP secretion in AscP/Fe^{2+}/TCPP@CNP(+) treated 4T1 breast cancer cells was improved by 2.72-, 4.34- and 4.23-fold *versus* that of Fe^{2+}/TCPP@CNP(+), respectively. Collectively, these data confirmed the efficacy of scP/Fe^{2+}/TCPP@CNP in inducing ICD of the cancer cells, which was ascribing to the enhanced ferroptosis arising from the conversion of H_2O_2 from $^1O_2$.

The efficient and specific distribution of AscP/Fe^{2+}/TCPP@CNP to tumor tissue was evaluated in 4T1 tumor-bearing mice model. As the *in vivo* images shown (Fig. 4a), comparing with free TCPP, the red fluorescence signal from nanoparticle was obviously detected at the tumor site and exhibited a typical time-dependent accumulation profile with the maximum fluorescence intensity at 24 h post-injection (i.v.). Meanwhile, the quantitative analysis result based on the *ex vivo* images (Fig. 4b, Fig. S6 in Supporting information) showed that the fluorescence intensity of TCPP in tumor tissues was enhanced 4.22-fold by AscP/Fe^{2+}/TCPP@CNP treatment *versus* that of free TCPP, demonstrating the superior tumor targeting ability of the nanoparticle.

The *in vivo* antitumor efficacy of AscP/Fe^{2+}/TCPP@CNP results (Figs. 4c–e) shown AscP@CNP exhibited negligible tumor inhibition effect compared with the control group. AscP/Fe^{2+}/TCPP@CNP(+) showed the strongest suppression effect with the tumor inhibition rate (TIR) of 75.42% ± 10.49%, which was significantly higher than Fe^{2+}/TCPP@CNP(+) (53.63% ± 9.55%, $P < 0.01$) and Fe^{2+}/TCPP@CNP(-) (28.11% ± 6.75%, $P < 0.001$). In addition, hematoxylin and eosin (H&E) and Ki67 staining sections of tumor tissues after AscP/Fe^{2+}/TCPP@CNP(+) treatment revealed the most extensive cells damage and proliferation negative signal (Fig. 4f). These results were consistent with the *in vitro* cytotoxicity data (Fig. 2d), both confirmed the enhancement of anti-tumor efficacy of the nanoparticle.

Ferroptosis hallmarks of malonaldehyde (MDA) and H_2O_2 level within tumor tissue were further investigated, respectively. As shown in Figs. 4g and h, AscP/Fe^{2+}/TCPP@CNP(+) treatment resulted in the highest intra-tumoral MDA and H_2O_2 level, which was enhanced by 1.43-fold and 1.48-fold *versus* that of Fe^{2+}/TCPP@CNP(+). Notably, Fe^{2+}/TCPP@CNP(-) and Fe^{2+}/TCPP@CNP(+) treatment produced similar MDA and H_2O_2 level compared to the control ($P < 0.001$), ascribing to the Fe^{2+} catalyzed Fenton reaction. These results proved the H_2O_2 self-supplying capacity of the nanoparticle by taking advantage of the conversion of H_2O_2 from $^1O_2$ generated by PDT, thereby boosting ferroptosis.

The *in vivo* ICD induction and anti-tumor immune response activation effect of AscP/Fe^{2+}/TCPP@CNP was further investigated. Immunostaining images of tumor tissues (Fig. 4i) showed that AscP/Fe^{2+}/TCPP@CNP(+) treatment caused the highest CRT exposure and lowest HMGB1 restriction in nuclei, followed by Fe^{2+}/TCPP@CNP(+) and Fe^{2+}/TCPP@CNP(-). Meanwhile, AscP/Fe^{2+}/TCPP@CNP(+) produced the highest level of matured DC in tumor infiltrating lymph nodes (TILNs) (Fig. 4j, Fig S7 in Supporting information), much more $CD8^+$ T cells infiltration inside tumor tissue (Fig. 4i), significantly enhanced interferon-γ (IFN-γ) secretion (Fig. 4k) comparing with Fe^{2+}/TCPP@CNP(+) and Fe^{2+}/TCPP@CNP(-). Collectively, these data confirmed that AscP/Fe^{2+}/TCPP@CNP could effectively induce ICD effect *in vivo* due to the enhanced ferroptosis.

The biosafety assay of AscP/Fe^{2+}/TCPP@CNP was measured in healthy mice. The histological examination results indicated there was no histological change in heart, liver, spleen, lung and kidney after nanoparticle treatment (Fig. S8a in Supporting information). The hepatorenal function evaluation and blood routine examination results shown that all the parameters were barely impacted by AscP/Fe^{2+}/TCPP@CNP (Figs. S8b and c in Supporting informa-

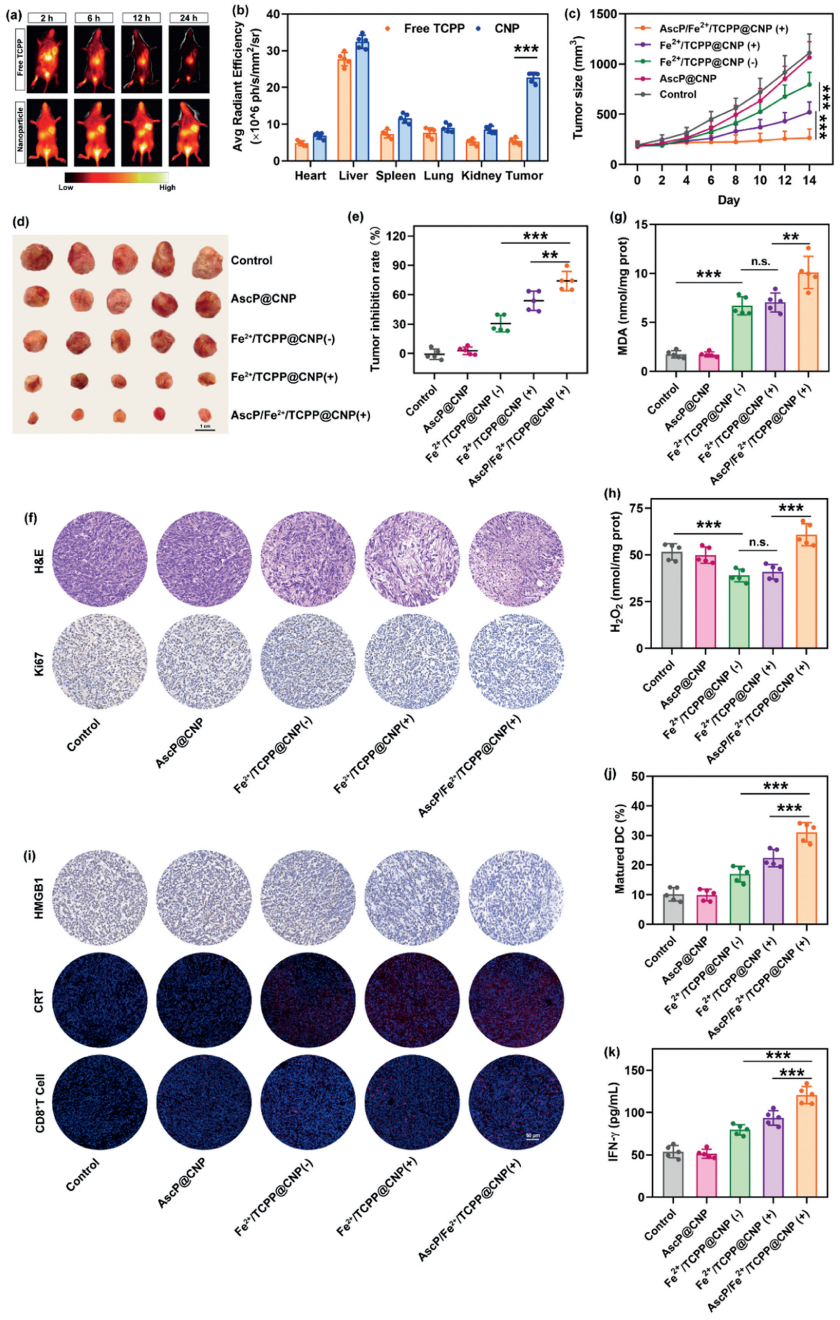

Fig. 4. Evaluation of tumor targeting ability and *in vivo* therapeutic efficacy for AscP/Fe^{2+}/TCPP@CNP. (a) *In vivo* images of 4T1 tumor-bearing BALB/c mice at 2, 6, 12 and 24 h post-injection (i.v.) of free TCPP and AscP/Fe^{2+}/TCPP@CNP, respectively. (b) Quantitative analysis result based on the *ex vivo* images of the major organs and tumor tissue at the timepoint of 12 h ($n = 5$). (c) 4T1 tumor growth curve during treated by different nanoparticles. (d) Digital photos of excised 4T1 tumor tissues after treatments (scale bar: 1 cm). (e) Tumor inhibition rates of 4T1 tumor-bearing mice after different treatments ($n = 5$). (f) The H&E and Ki67 stain for the tumor tissues at the end of experiment (scale bar: 50 μm). Intra-tumoral level of MDA (g) and H_2O_2 (h) at the end of treatment ($n = 5$). (i) CRT, HMGB1 and $CD8^+$ T cells staining within the tumor tissues (scale bar: 50 μm). (j) Quantitative analysis of maturated DCs in TILNs by FCM ($n = 5$). (k) IFN-γ level within tumor tissues analyzed by enzyme linked immunosorbent assay (ELISA) ($n = 5$). Data are presented as mean ± SD. $^{**}P < 0.01$, $^{***}P < 0.001$.

tion) In addition, there was no significant body weight loss of the tumor-bearing mice during the therapeutic efficacy evaluation (Fig. S9 in Supporting information). Taken together, these data indicated the good biocompatibility of AscP/Fe^{2+}/TCPP@CNP.

In summary, we successfully developed a novel H_2O_2 self-supplying coordination-assembled nanoparticle based on the pH-responsive lipopeptide C_{18}-pHis_{10} to co-encapsulate AscP, Fe^{2+}, and TCPP. In which, Fe^{2+} and TCPP were encapsulated into the lipopeptide assemblies by coordinate interaction with His, which mimicked the coordinate pattern of hemoglobin binding heme. The functionalized lipopeptide could respond to the acidic endo-lysosome environment, causing the breakage of Fe^{2+}/His/TCPP coordinate interaction and subsequent fast release of payloads. *In vitro* and *in vivo* results demonstrated that TCPP produced excessive $^1O_2$ upon laser irradiation, the generated $^1O_2$ could be reduced to H_2O_2 by AscP for further catalyzed to more lethal $^{\bullet}OH$ by Fe^{2+} *via* Fenton reaction, leading to enhanced ferroptosis. Collectively, this study proposed a novel H_2O_2 self-supplying approach by taking advantage of the conversion of H_2O_2 from $^1O_2$ generated by PDT to boost ferroptosis.

Declaration of competing interest

The authors declare that they have no known competing financial interests or personal relationships that could have appeared to influence the work reported in this paper.

CRediT authorship contribution statement

Yan Gao: Writing – original draft, Visualization, Software, Methodology, Investigation, Funding acquisition, Formal analysis, Conceptualization. **Zi-Lin Song:** Validation, Software, Methodology, Investigation, Data curation. **Shuang Yu:** Validation, Software, Investigation, Data curation. **Xiu-Li Zhao:** Supervision, Project administration, Funding acquisition, Conceptualization. **Da-Wei Chen:** Supervision, Resources, Funding acquisition, Conceptualization. **Ming-Xi Qiao:** Writing – review & editing, Supervision, Resources, Funding acquisition, Conceptualization.

Acknowledgments

The authors are grateful to the funding of National Natural Science Foundation of China (Nos. 82304426 and 81573372), Postdoctoral Fellowship Program of CPSF (No. GZC20231730), Career Development Support Plan for Young and Middle-aged Teachers in Shenyang Pharmaceutical University (No. ZQN2014A03).

Supplementary materials

Supplementary material associated with this article can be found, in the online version, at doi:10.1016/j.cclet.2024.110097.

References

[1] B.R. Stockwell, Cell 185 (2022) 2401–2421.
[2] Y. Du, Z. Guo, Cell Death Discov. 8 (2022) 501.
[3] J.P.F. Angeli, D.V. Krysko, M. Conrad, Nat. Rev. Cancer 19 (2019) 405–414.
[4] C. Liu, S. Sun, Q. Feng, et al., Adv. Mater. 33 (2021) e2102054.
[5] Y. Wang, C. Zhang, S. Han, et al., Chin. Chem. Lett. 35 (2024) 109578.
[6] H. Liu, T. Nie, X. Duan, et al., J. Control. Release 359 (2023) 132–146.
[7] C. Liu, Q. Shi, X. Huang, et al., Nat. Rev. Cancer 23 (2023) 526–543.
[8] Y. Zhuang, S. Han, Y. Fang, et al., Coord. Chem. Rev. 455 (2022) 214360.
[9] T. Liu, Y. Li, J. Lau, et al., ACS Nano 12 (2018) 11355–11365.
[10] Z. Tang, P. Zhao, H. Wang, et al., Chem. Rev. 121 (2021) 1981–2019.
[11] C. Jia, Y. Guo, F.G. Wu, Small 18 (2022) e2103868.
[12] H.J.H. Fenton, H.O. Jones, J. Chem. Soc. Trans. 77 (1900) 69–76.
[13] D. Tang, X. Chen, R. Kang, G. Kroemer, Cell Res. 31 (2021) 107–125.
[14] G. Lei, L. Zhuang, B. Gan, Nat. Rev. Cancer 22 (2022) 381–396.
[15] L. Li, B. Sun, J. Sun, et al., Chin. Chem. Lett. 35 (2024) 109538.
[16] Y. Yu, Y. Meng, X. Xu, et al., ACS Nano 17 (2023) 3334–3345.
[17] B. Yang, Y. Chen, J. Shi, Chem. Rev. 119 (2019) 4881.
[18] E.C. Cheung, K.H. Vousden, Nat. Rev. Cancer 22 (2022) 280.
[19] X. Meng, X. Zhang, M. Liu, et al., Appl. Mater. Today 21 (2020) 100864.
[20] T. Yang, M. Zhou, M. Gao, et al., Small 19 (2023) 2205692.
[21] C. Liu, J. Xing, O.U. Akakuru, et al., Nano Lett. 19 (2019) 5674–5682.
[22] H. Zhou, X. Li, D. Niu, et al., Adv. Healthc. Mater. 10 (2021) e2002126.
[23] F. Deng, H. Olvera-Vargas, M. Zhou, et al., Chem. Rev. 123 (2023) 4635–4662.
[24] Y. Zhou, S. Fan, L. Feng, et al., Adv. Mater. 33 (2021) e2104223.
[25] Y. Zhu, R. Zhu, Y. Xi, et al., Appl. Catal. B 255 (2019) 117739.
[26] Z. Chu, J. Yang, W. Zheng, et al., Coord. Chem. Rev. 481 (2023) 215049.
[27] H. Ranji-Burachaloo, P.A. Gurr, D.E. Dunstan, G.G. Qiao, ACS Nano 12 (2018) 11819–11837.
[28] W.P. Li, C.H. Su, Y.C. Chang, et al., ACS Nano 10 (2016) 2017–2027.
[29] B. Lee, O.K. Park, L. Pan, et al., Adv. Mater. 35 (2023) e2305512.
[30] Y. Zhang, P.H. Chen, B. Li, et al., ACS Nano 17 (2023) 16743–16756.
[31] C. Liu, J. Yao, J. Hu, et al., Mater. Horiz. 7 (2020) 3176–3186.
[32] S. Gao, Y. Jin, K. Ge, et al., Adv. Sci. 6 (2019) 1902137.
[33] S. Kwon, H. Ko, D.G. You, et al., Acc. Chem. Res. 52 (2019) 1771.
[34] Y. Dai, Z. Yang, S. Cheng, et al., Adv. Mater. 30 (2018) 2753–2765.
[35] S. Wang, G. Yu, Z. Wang, et al., Angew. Chem. 131 (2019) 14900–14905.
[36] L. Lin, S. Wang, H. Deng, et al., J. Am. Chem. Soc. 142 (2020) 15320–15330.
[37] S. Liang, X. Xiao, L. Bai, et al., Adv. Mater. 33 (2021) 2100333.
[38] X. Zhong, X. Wang, L. Cheng, et al., Adv. Funct. Mater. 30 (2020) 1907954.
[39] G. Li, S. Wang, D. Deng, et al., ACS Nano 14 (2020) 1586–1599.
[40] G. Li, S. Yuan, D. Deng, et al., Adv. Funct. Mater. 29 (2019) 1901932.
[41] L. Shen, T. Zhou, Y. Fan, et al., Chin. Chem. Lett. 31 (2020) 1709–1716.
[42] N. Yang, W. Xiao, X. Song, et al., Nano-Micro Lett. 12 (2020) 1–27.
[43] C. Liu, J. Shin, S. Son, et al., Chem. Soc. Rev. 50 (2021) 2260–2279.
[44] C. Liu, L. Luo, L. Zeng, et al., Small 14 (2018) e1801851.
[45] Y. Wang, C. Wu, C. Feng, et al., Chin. Chem. Lett. 36 (2025) 109902.
[46] Y. Wang, Y. Lin, S. He, et al., J. Hazard. Mater. 461 (2023) 132538.
[47] J. Cheng, S. Wan, S. Cao, Angew. Chem. Int. Ed. 62 (2023) e202310476.
[48] T.A. Mishchenko, I.V. Balalaeva, M.V. Vedunova, D.V. Krysko, Trends Cancer 7 (2021) 484–487.
[49] X. Meng, J. Deng, F. Liu, et al., Nano Lett. 19 (2019) 7866–7876.
[50] Y. Zhou, K. Chen, W.K. Lin, et al., Adv. Healthc. Mater. 12 (2023) 2370170.
[51] Z. Jing, Y. Li, J. Song, X. Zang, Int. J. Biol. Macromol. 25 (2023) 126912.
[52] Y. Gao, Z. Song, L. Jia, et al., Biomaterials 291 (2022) 121902.
[53] M.S. Liao, M.J. Huang, J.D. Watts, J. Phys. Chem. A 114 (2010) 9554–9569.
[54] X. Bai, Y. Huang, M. Lu, D. Yang, Angew. Chem. Int. Ed. 56 (2017) 12873–12877.